Title

Cooperativity of $K_V7.4$ channels confers ultrafast electromechanical sensitivity and emergent properties in cochlear outer hair cells.

Journal

Science advances, 6(15)

ISSN

2375-2548

Authors

Perez-Flores, Maria C
Lee, Jeong H
Park, Seojin
et al.

Publication Date

2020-04-01

DOI

10.1126/sciadv.aba1104

Peer reviewed

HEALTH AND MEDICINE

Cooperativity of $K_v7.4$ channels confers ultrafast electromechanical sensitivity and emergent properties in cochlear outer hair cells

Maria C. Perez-Flores[1]*, Jeong H. Lee[1]*, Seojin Park[1], Xiao-Dong Zhang[2,3], Choong-Ryoul Sihn[1], Hannah A. Ledford[2], Wenying Wang[1], Hyo Jeong Kim[1], Valeriy Timofeyev[2,3], Vladimir Yarov-Yarovoy[4], Nipavan Chiamvimonvat[2,3], Richard D. Rabbitt[5†], Ebenezer N. Yamoah[1†]

The mammalian cochlea relies on active electromotility of outer hair cells (OHCs) to resolve sound frequencies. OHCs use ionic channels and somatic electromotility to achieve the process. It is unclear, though, how the kinetics of voltage-gated ionic channels operate to overcome extrinsic viscous drag on OHCs at high frequency. Here, we report ultrafast electromechanical gating of clustered $K_v7.4$ in OHCs. Increases in kinetics and sensitivity resulting from cooperativity among clustered-$K_v7.4$ were revealed, using optogenetics strategies. Upon clustering, the half-activation voltage shifted negative, and the speed of activation increased relative to solitary channels. Clustering also rendered $K_v7.4$ channels mechanically sensitive, confirmed in consolidated $K_v7.4$ channels at the base of OHCs. $K_v7.4$ clusters provide OHCs with ultrafast electromechanical channel gating, varying in magnitude and speed along the cochlea axis. Ultrafast $K_v7.4$ gating provides OHCs with a feedback mechanism that enables the cochlea to overcome viscous drag and resolve sounds at auditory frequencies.

INTRODUCTION

Among the remarkable features of the mammalian auditory system is its unparalleled speed. Second-order neurons in the auditory brainstem can detect submillisecond interaural timing differences (*1*), which requires each ear to transmit action potentials to the central nervous system at precise times relative to peaks in the sound waveform over a broad range of intensities. Cochlear outer hair cells (OHCs) are key to this process, endowing the mammalian ear with a fast electromechanical amplification mechanism essential to the dynamic range and speed of sound encoding. OHCs are capable of generating cycle-by-cycle force (*2*) at auditory frequencies exceeding 50 kHz [(*3*), cf. (*4*)], but how this is achieved given the intrinsic biophysical properties of the cell and whether cycle-by-cycle amplification occurs in the living cochlea remain unclear (*5*).

The OHC somatic electromechanical motor draws power from voltage-driven charge displacement (*6*) and requires the expression of the protein prestin in the cell membrane to function (*7*). The first stage of transduction is achieved through the direct mechanical gating of mechanoelectrical transduction (MET) channels in the stereocilia (*8*), which modulates the input transduction current at auditory frequencies (*9*). When cationic current enters the cell, the membrane depolarizes, driving a piezoelectric-like shortening of the cell and converting electrical input into mechanical output (*10*). This OHC electromechanical motor is the primary mechanism underlying sound-driven amplification in the cochlea (*11*, *12*). The shortening of OHCs in response to MET currents is nearly constant for low-frequency stimuli but begins to decline for frequencies above the electromechanical corner frequency of the cell—a frequency set in part by the capacitance and conductance of the OHC at the resting membrane potential (*6*, *13*). The corner frequency is unusually high in OHCs relative to most excitable cells, primarily due to the expression of the K^+ channel $K_v7.4$, which introduces a large conductance, and concomitant current (I_{Kn}), at the cell resting potential (*14*, *15*). Although the contribution of $K_v7.4$ channels to the tonic conductance and corner frequency is clear (*13*), it is not known whether the channels also contribute to OHC function at auditory frequencies on a cycle-by-cycle basis.

Here, we report ultrafast electromechanical gating of $K_v7.4$ in murine cochlear OHCs that develops with hearing as channel density in the basal pole of the cell increases. Analogous increases in speed and mechanosensitivity were observed when clustering was artificially induced in a model cell line using an optogenetic approach (*16*, *17*), suggesting that physical interaction between channels coordinates gating (*18*). Results demonstrate that $K_v7.4$ channel cooperativity enhances kinetics and mechanosensitivity relative to solitary channels and endows OHCs with the ability to respond to changes in voltage and mechanical stress on a cycle-by-cycle basis at auditory frequencies. Simulations of OHC electromechanical function in the context of the cochlear load further indicate that $K_v7.4$ cooperativity and the ensuing mechanosensitivity extend the bandwidth and tune the frequency-dependent power efficiency of OHCs to match the tonotopic map in the cochlea—features that may be essential to the emergent frequency selectivity and sensitivity of the active cochlea.

RESULTS

Consolidation of $K_v7.4$ channels at the basal pole of OHCs parallels the maturation of channel kinetics

We hypothesized that consolidation of $K_v7.4$ channels at the basal pole of OHCs is required for cooperativity, and therefore, we expected increases in channel clusters to occur in parallel with maturation of

[1]Department of Physiology, School of Medicine, University of Nevada, Reno, Reno, NV 89557, USA. [2]Department of Internal Medicine, Division of Cardiology, University of California, Davis, Davis, CA 95616, USA. [3]Department of Veterans Affairs, Northern California Health Care System, Mather, CA 95655, USA. [4]Department of Physiology and Membrane Biology, University of California, Davis, Davis, CA 95616, USA. [5]Departments of Biomedical Engineering, Otolaryngology, and Neuroscience Program, University of Utah, Salt Lake City, UT 84112, USA.
*These authors contributed equally to this work.
†Corresponding author. Email: enyamoah@gmail.com (E.N.Y.); r.rabbitt@utah.edu (R.D.R.)

the associated ionic current I_{Kn} (*14*). Channel clustering was monitored as the fractional ratio (cluster area/OHC surface area) during the development of hearing in mice using immunolabeling in OHCs located along the cochlear tonotopic map, representing characteristic frequencies (CFs) from 2 to 10 kHz (Fig. 1A). Before the onset of hearing, $K_v7.4$ channels were dispersed spatially along the basolateral membrane of OHCs [postnatal day 4 (P4) and P8; Fig. 1, B and C]. With the maturation of hearing, the channels consolidated into tight clusters at the basal pole of OHCs (P24; Fig. 1D). In mature cochleae, the cluster area (Fig. 1E) and the puncta density (Fig. 1F) both increased along the tonotopic axis of the cochlea from apex to base, suggesting a role for $K_v7.4$ expression and clustering in the frequency response of OHCs.

The kinetics of I_{Kn} developed in parallel with the formation of $K_v7.4$ clusters at the basal pole of OHCs. At P8, outward K^+ currents in OHCs at the 3- to 4-kHz location exhibited a Boltzmann function half-activation voltage $V_{1/2} = -33.6 \pm 1.0$ mV and a voltage sensitivity at half-activation of $56.5 \pm 5.1\ V^{-1}$ (P8, $n = 15$; Fig. 2, A and C). By P24, the half-activation shifted negative $V_{1/2} = -81.1 \pm 1.7$ mV, and the sensitivity increased to $97.1 \pm 6.0\ V^{-1}$ (P24, $n = 17$; Fig. 2, B and C). The activation time constant reduced three- to eightfold from P8 and P24 (fig. S1). Blocking with linopirdine (lino) and XE991 confirmed that a majority of this outward current was due to $K_v7.4$ (*19*, *20*). In mature mice (P24), both kinetics and voltage sensitivity at half-activation changed with location along with the tonotopic map and associated changes in channel density. Most notably, the voltage sensitivity, which reflects the effective gating charge, increased along the low-to-high frequency axis of the cochlea (Fig. 2D, blue) and the activation time constant (τ_{act}) decreased (Fig. 2E, blue). After $K_v7.4$ clustering at the basal pole (P24), I_{Kn} exhibited high-temperature sensitivity (Fig. 3A), and activation kinetics increased with CF along with the tonotopic map in the cochlea. Temperature and voltage dependence is shown for OHCs located at ~2 kHz CF location (Q_{10} ~ 2.3; Fig. 3, B and C). Kinetics increased with CF location from apex to base at 30°C and, when extrapolated to 37°C, exhibited submillisecond time constants (Fig. 3C).

$K_v7.4$ cooperativity is revealed by inducing high channel density in HEK cells

We expressed mouse $K_v7.4$ channels in the human embryonic kidney (HEK) 293 cells and used an optogenetic strategy to induce clustering. A system to coalesce channels was constructed by fusing the

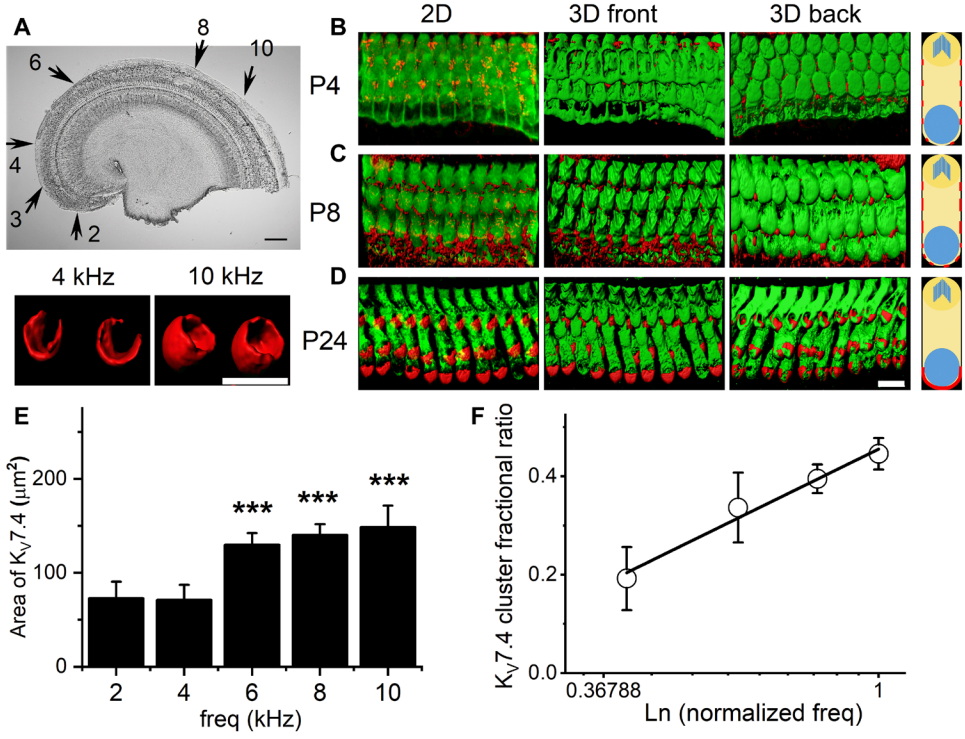

Fig. 1. $K_v7.4$ clusters increased in OHCs along the frequency-place map of the mammalian cochlear. (**A**) Representative segment of the mouse cochlea, showing the approximate frequency-place map from apical to basal contour (arrows). The black arrows indicate the predicted labeled sound frequencies (in kilohertz), represented on the cochlear map. Scale bar, 100 μm. (**B** to **D**) The expression pattern of $K_v7.4$ channels in OHCs from P4 (B), P8 (C), and P24 (D), respectively. Scale bar in (D) [representing (B) to (D)], 10 μm. The left panel represents two-dimensional (2D) confocal sections. Hair cells were labeled with myosin 7A antibody (Alexa Fluor 488 or fluorescein isothiocyanate in green) and $K_v7.4$ antibody (Alexa Fluor 555 in red). The middle and right panels show a 3D rendition of Z-stack images representing the front and back of the images, respectively, to locate $K_v7.4$ expression. Shown in the right panel are schematic representations summarizing channel expression during development. (**E**) By P24, when there are defined $K_v7.4$ clusters at the basolateral region of OHCs across the frequency-place map of the cochlea, semiquantitative analysis of the surface area of clusters was performed using the Imaris software routine and plotted against the apparent location and frequency representation of OHCs. The inset (above) shows examples of $K_v7.4$ clusters used to measure the areas shown in the bar graph. Scale bar, 4 μm. Data were generated from 50 OHCs from each frequency location and averaged from 12 different cochleae. Data were compared to OHCs at the apical tip of the cochlea (2 kHz) (***$P < 0.001$). (**F**) $K_v7.4$ fractional ratio was estimated as the area of $K_v7.4$ cluster/OHC surface area. The relation between the $K_v7.4$ cluster ratio along the frequency-place map of the cochlea was best described with a natural logarithmic function of the normalized frequency, from 2 to 10 kHz, where 10 kHz was set as 1. The data represent a onefold increase in channel fractional cluster ratio per octave.

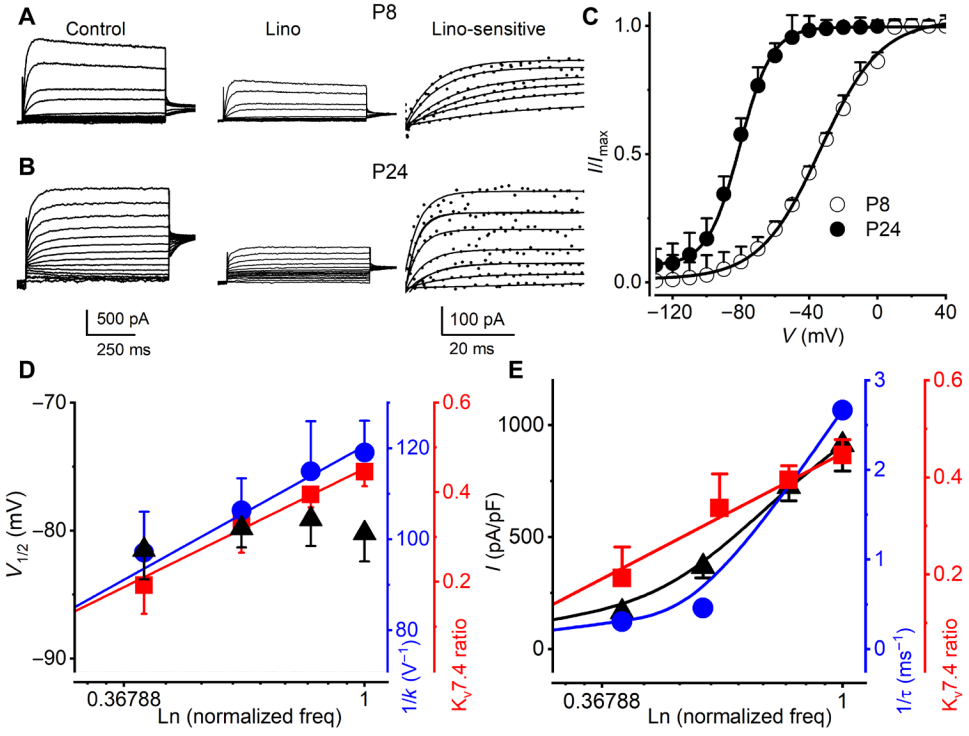

Fig. 2. Outward K^+ currents in mouse OHCs show sensitivity toward lino and a profound negative shift in the steady-state voltage-dependent activation and fast onset of activation time constant (τ_{act}) during development. The linopirdine (lino)–sensitive current (I_{Kn}) in OHCs increases in density and shows a smaller τ_{act} as $K_v7.4$ cluster density increases. (**A** and **B**) Currents elicited in response to voltage steps in P8 to P24 OHCs from mice were recorded from the cochlear location at CF of 3 to 4 kHz. Currents were elicited by applying voltage steps from −130 mV with increasing voltage steps in 10-mV increments. Deactivation voltage steps were at −30 mV. The sensitivity of the current was tested with 200 μM lino, and the difference current (in dotted plots) was fitted with one exponential function shown in solid lines to obtain time constants of activation (τ_{act}). (**C**) Current density (*I*)–voltage (*V*) relations fitted with a single Boltzmann function of the form $I(V) = I_{max}/[1 + \exp.(-(V - V_{1/2}))/k]$, where I_{max} is the maximum current density, *V* is the membrane voltage, $V_{1/2}$ is the half-activation voltage, and $1/k$ is the voltage sensitivity at half-activation. The $V_{1/2}$ (in mV) and $1/k$ (in V^{-1}) for the currents at P8 and P24 were −33.6 ± 1.0 and 56.5 ± 5.1 ($n = 15$) and −81.1 ± 1.7 and 97.1 ± 6.0 ($n = 17$), respectively. Comparing $V_{1/2}$ and $1/k$ at P8 and P24 currents ($V_{1/2}$, $P < 0.0001$ and $1/k$, $P < 0.0001$). (**D**) Relations between $V_{1/2}$ of I_{Kn} in P24 OHCs at different cochlear locations, showing no visible changes (▲). The voltage sensitivity at half-activation of I_{Kn} increased relative to frequency by 18 V^{-1} kHz^{-1} (●) and $K_v7.4$ fractional area ratio (■) as a function of CFs of OHCs. (**E**) I_{Kn} voltage dependence in P24 mouse OHCs from different frequency-place maps of the cochlea, representing CFs (in kHz) 2, 4, 6, and 10. Relations between the maximum current density (▲) measured in pA/pF, τ_{act} of currents at 0 mV (●), and fractional area ratio (●) as a function of CFs are shown for comparison.

$K_v7.4$ N terminus with truncated CIB1 (CIBN) and coexpressing with CIBN-cryptochrome 2 (CRY2) (*17*). In this system, exposure to blue light (488 nm) mediates oligomerization of the N termini CIBN-EGFP-$K_v7.4$ channel subunits, while enhanced green fluorescent protein (EGFP) and mCherry served as reporters (Fig. 4A; see also fig. S2). Cotransfection, followed by exposure to blue light, induced clustering (fig. S2). Clustering was confirmed by fluorescence recovery after photobleaching (FRAP), which showed dynamic recruitment of CIBN-EGFP-$K_v7.4$ and CRY2-mCherry with a time constant of ~1.4 ± 0.6 and 1.0 ± 0.4 min (n = 9), respectively, compared to a recovery time constant of EGFP alone, 0.2 ± 0.1 min (n = 5) (Fig. 4B). For cells transfected with CIBN-EGFP-$K_v7.4$ and CRY2-mCherry, a family of voltage steps elicited outward currents with delayed activation kinetics (*21*) (fig. S2). In contrast, after ~4 min of blue-light exposure, current traces showed visibly increased onset and deactivation kinetics (Fig. 4C). Blue-light exposure shifted the voltage activation negative ~8 mV and increased the speed by two- to eightfold (Fig. 4, D and E), while current amplitude [maximum current density (pA/pF)] did not change significantly; 72.8 ± 19.9 versus 74.5 ± 16.8 (n = 18; P = 0.8), respectively. Voltage sensitivity (Fig. 4D) was determined from tail currents for finite length voltage commands. We varied the exposure time to assess time-dependent changes in the τ_{act} (Fig. 4F and inset). The slow activation became increasingly faster as the duration of blue-light exposure increased, while the steady-state current amplitude remained unchanged [current density at 0 mV was 48.4 ± 12.6 before and 51.1 ± 17.2 (pA/pF) after blue-light illumination, $n = 21$; $P = 0.6$]. Changes in kinetics with blue-light exposure demonstrate the cooperativity of $K_v7.4$ channels when expressed in high density.

The cooperativity hypothesis is also supported by changes in the apparent gating charge movement and estimates of the number of independent channel units. We measured the gating current in CIBN-EGFP-$K_v7.4$ and CRY2-mCherry cotransfected cells before and after blue-light exposure to determine voltage dependence of charge movements (*Q*-*V* curve) (Fig. 4G). Blue-light exposure shifted the *Q*-*V* half to the left from −40.9 ± 2.1 to −45.7 ± 2.4 (mV, n = 7; $P < 0.002$) and increased the voltage sensitivity at half-activation from 59.7 ± 7.4 to 97.2 ± 19.1 (V^{-1}, $n = 7$; $P < 0.0004$). The difference in the transition Gibbs free energy (*22*) in clustered versus solitary states was −1.1 ± 0.2 kcal/mol ($n = 7$), suggesting cluster-driven cooperativity that may favor specific closed state(s). This implication was further supported by nonstationary fluctuation analysis. The variance of

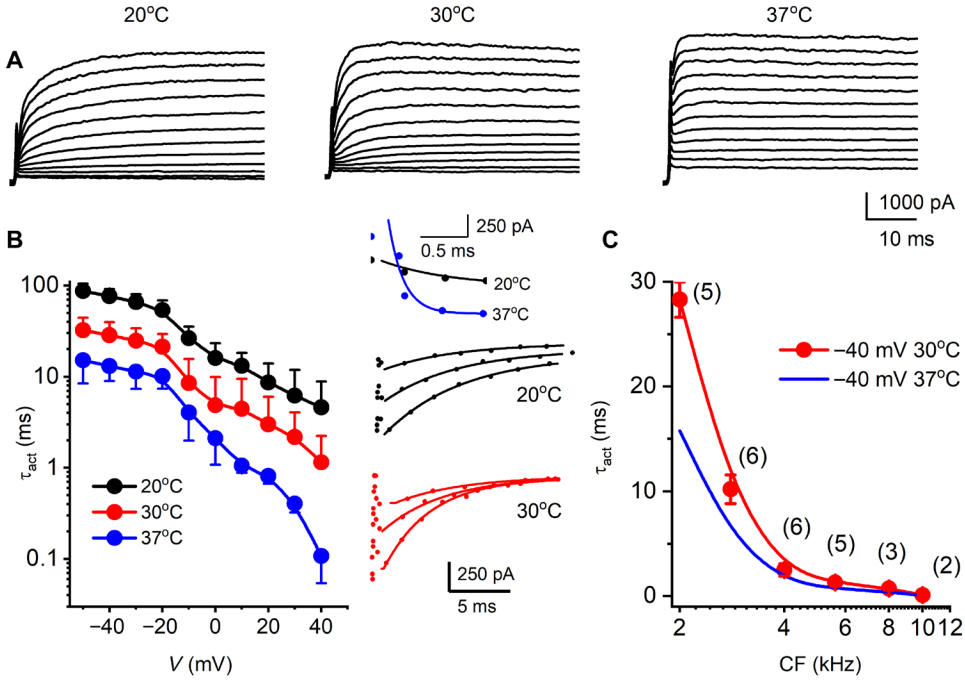

Fig. 3. Activation and deactivation kinetics of I_{Kn} in OHCs at different temperatures, cochlear locations, and CFs. (**A**) Family of I_{Kn} traces recorded from an OHC located at a 2-kHz frequency-place map of a 24-day-old mouse cochlea at room temperature (20°C, left), 30°C (middle), and physiological temperature (37°C, right). Currents were elicited from a holding voltage of −120 mV, and the voltage steps ranged from −120 to 50 mV with $\Delta V = 10$ mV. The deactivation test voltage was at −30 mV (not shown). (**B**) Relations between activation time constants (τ_{act}) and voltages at 20°C (●), 30°C (●), and 37°C (●). The activation kinetics were fitted with a single exponential function [see insets in the right panel for examples of fitted traces of activation (top) and deactivation (bottom)]. Summary data were obtained from 3- to 4-kHz OHCs from five cochleae ($n = 14$). The data represent recordings in which three temperatures (20°, 30°, and 37°C) were successfully achieved from the same OHCs. The Q_{10} of I_{Kn}, which was expressed as $(\tau_2/\tau_1)^{(10/T_2-T_1)}$ where T is temperature and τ is the time constant of activation, was 2.3. (**C**) Summary data for τ_{act} of I_{Kn} generated at a step voltage of −40 mV from OHCs at different CFs of the cochlea at 30°C (●); $n = 27$ cochleae. The number of OHCs for each data point is indicated (●), and the extrapolated τ_{act} at 37°C was obtained using $Q_{10} = 2.3$ (solid blue line).

~200 gating current sweeps showed a parabolic profile with a leftward shift in the gating current fluctuations as a function of mean current following blue-light exposure (Fig. 4H). If the unitary gating charge remained unchanged, the leftward shift suggests a reduction in the apparent number of functional channel units in the membrane, consistent with the induction of cooperativity by clustering of the channels.

$K_v7.4$ mechanosensitivity emerges with cooperativity

In mature cochleae, consolidated $K_v7.4$ clusters are located between the OHC lateral wall motor and adjacent Deiters' cell and are subject to mechanical forces during electromotility. We examined the mechanosensitivity of $K_v7.4$ channels in HEK 293 cells by recording changes in I_{Kn} resulting from blunt probe ~0.6-μm mechanical indentation of the plasma membrane. Mechanosensitivity was not detected in HEK cell expressing solitary channels in control conditions (Fig. 5, A to C). In contrast, in CIBN-EGFP-$K_v7.4$ plus CRY2-mCherry cotransfected cells, mechanosensitivity emerged after inducing clustering by blue-light exposure (Fig. 5, D to F, green versus blue). After clustering of $K_v7.4$, application of mechanical stress increased the peak voltage-evoked current (Fig. 5, D and E, green) and shifted half-activation voltage leftward ~32 ± 3 mV ($n = 7$) (Fig. 5F). The increase in peak current evoked by stress was over and above the peak current that could be evoked by voltage. Although alternative explanations are possible, the transition state model introduced below suggests that mechanosensitivity may arise from a late conformational transition, after transitions responsible for voltage sensitivity pose $K_v7.4$ channels for stochastic opening (fig. S4).

On the basis of results in HEK cells, we hypothesized that I_{Kn} in OHCs would become mechanically sensitive as $K_v7.4$ channels clustered during maturation of hearing. To test this idea, mechanical sensitivity in OHCs located at the ~3- to 4-kHz place map in the cochlea at P6 (before clustering) was compared to P21 (after clustering). For the example shown (Fig. 5G), the OHC basolateral membrane was indented by ~0.4 μm while maintaining a gigohm seal at the recording electrode. The outward current density and time constant of onset recorded in P6 OHCs were not altered by the mechanical somatic indentation (Fig. 5G). In sharp contrast, in P21 OHCs, the same mechanical stimulus resulted in a ~1.3-fold increase in current magnitude and ~15 ± 4 mV leftward shift in the half-activation voltage (Fig. 5, H and I). The opposite was found when removing the resting turgor pressure and membrane stress in adult OHCs by applying a hypertonic extracellular solution (Fig. 5, J to L). The hypertonic solution did not alter the distribution of $K_v7.4$ in OHCs (fig. S3). Results demonstrate that $K_v7.4$ consolidated at the basal pole in mature OHCs develop mechanosensitivity.

Since prestin (Slc26a5) expression alters membrane tension in OHCs and changes I_{Kn} properties when cotransfected in Chinese hamster ovary cells (*23*), we predicted that I_{Kn} properties in the prestin null (*Slc26a5*$^{-/-}$) would differ from wild-type (*Slc26a5*$^{+/+}$) OHCs. Voltage-clamp recordings of I_{Kn} from P24 OHCs at 3- to 4-kHz cochlear location from *Slc26a5*$^{+/+}$ (fig. S4, A and B, black)

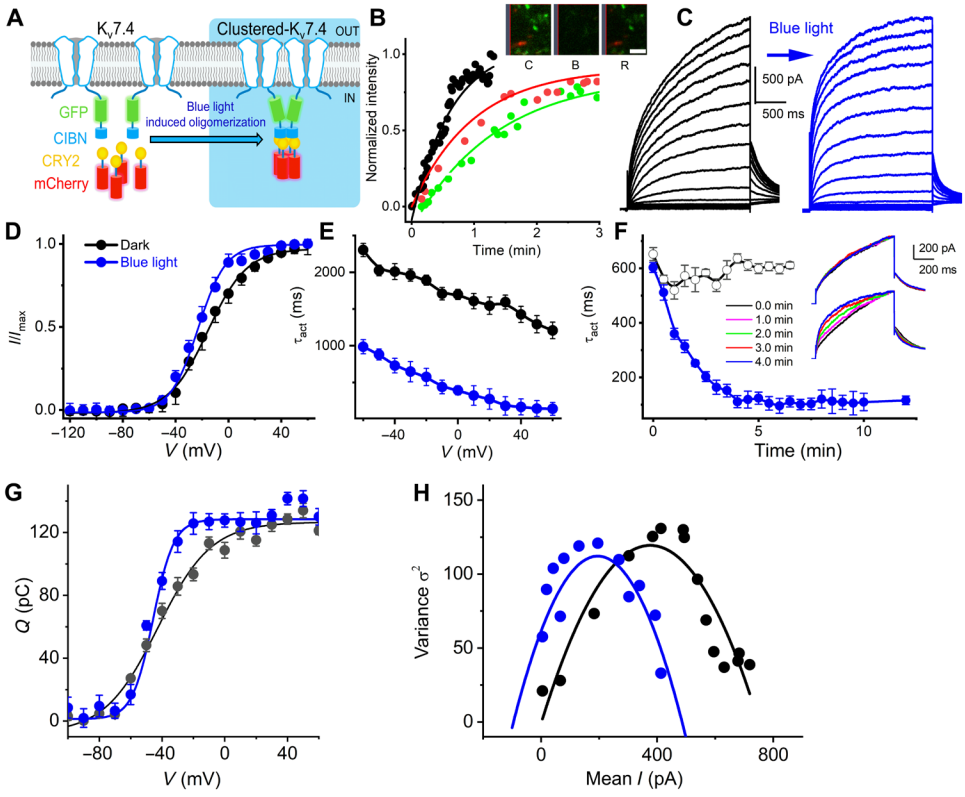

Fig. 4. Induction of $K_v7.4$ clusters by CRY2-CIBN optogenetic actuator strategy mediates changes in voltage dependence and time dependence of activation of $K_v7.4$ currents. (**A**) Graphic representation of blue light (488 nm)–induced oligomerization system with CIBN fused to the N terminus of $K_v7.4$. (**B**) Time course of CIBN-EGFP-$K_v7.4$ channel cell surface and CRY2-mCherry expression probed using live-cell imaging. FRAP experiments were performed in HEK 293 cells transfected with CIBN-EGFP-$K_v7.4$ channel and CRY2-mCherry plasmids. Sequential images of cells and region of interest (ROI) are shown for control (C), bleach (B), and recovery (R) after bleach (insets represent enlarged ROI). Relative fluorescence intensity of the ROI and the time course of recovery for CIBN-EGFP-$K_v7.4$ channel (green) and CRY2-mCherry (red). Scale bar, 1 μm. Time constants of recovery (τ) were as follows: CIBN-EGFP-$K_v7.4$ = 1.4 ± 0.6 min (n = 9) and CRY2-mCherry = 1.0 ± 0.4 min (n = 9). HEK 293 cells transfected with EGFP (black) and mCherry (not shown) alone had faster τ of recovery = 0.2 ± 0.1 and 0.1 ± 0.2 min (n = 5). Comparing the recovery τ of CIBN-EGFP-$K_v7.4$ and EGFP, $P < 0.001$; and CRY2-mCherry and mCherry, $P < 0.001$. (**C**) Typical current records from HEK 293 cells expressing CIBN-GFP-$K_v7.4$ and CRY2-mCherry before (black traces) and after 4-min pulse of blue-light exposure (blue trace). Noticeably, induction of channel clusters sped up the time course of activation, but the current magnitude remained unchanged [maximum current density (pA/pF) before (72.8 ± 19.9) and after (74.5 ± 16.8) blue-light illumination, n = 18, P = 0.8]. (**D**) The voltage dependence of normalized current density (I/I_{max}). Black (●) and blue (●) solid circles represent data generated from current records before and after blue-light exposure. Fits (in solid lines) of the voltage dependence of activation, using single Boltzmann function yielded the following: before blue light (in mV), $V_{1/2}$ = −15.1 ± 1.2, $1/k$ (V^{-1}) = 66.2 ± 3.9 (n = 14); 5 min after blue light, −23.0 ± 1.1, $1/k$ = 95.2 ± 4.7 (n = 14). Comparing $V_{1/2}$ and $1/k$ before and after blue-light exposure ($V_{1/2}$, $P < 0.0001$ and $1/k$, $P < 0.0001$). (**E**) Relations between activation time constant (τ_{act}), as a function of step voltages, show at least two- to eightfold reduction, depending on the voltage step, after blue-light exposure. (**F**) Summary data of blue-light exposure–time dependence of τ_{act} of CIBN-EGFP-$K_v7.4$ (○) and CIBN-EGFP-$K_v7.4$ + CRY2-mCherry (●) channels (n = 6 cells). The inset traces are representative of the summary data. Traces were elicited from −80-mV holding voltage and test voltage was 0 mV: [(in pA/pF) 48.4 ± 12.6 and 51.1 ± 17.2; n = 21, P = 0.6]. (**G**) Gating current records elicited in response to voltage steps from cells transfected with CIBN-EGFP-$K_v7.4$ and CRY2-mCherry. Gating currents were generated from a holding potential of −100 mV, using voltage steps ranging from −100 to 50 mV, ΔV = 10 mV. Integral of gating currents (Q) and the voltage dependence fitted by a single Boltzmann function before and after exposure to blue light. $V_{1/2}$ (mV) before and after blue light was −40.9 ± 2.1 and −45.7 ± 2.4 (n = 7, $P < 0.01$), and the voltage sensitivity at half-activation $1/k$ (V^{-1}) was 58.8 ± 4.1 and 93.6 ± 3.3 (n = 7, $P < 0.001$). (**H**) Nonstationary fluctuation analyses of gating current. Data from 200 consecutive gating current traces collected at 1-s intervals. The mean gating current as a function of variance plotted and fitted with the function $\sigma^2 = i.I - (I^2/N)$, where σ^2, i, I, and N represent variance, single gating charge current amplitude, macroscopic gating current, and the total number of channels, respectively. Estimates from the best fits for i and N before and after blue-light exposure were i = 0.06 ± 0.01 pA and 0.05 ± 0.02 pA (n = 4, P = 0.41), and N = 1177 ± 198 and 1002 ± 203 (n = 4, P = 0.26). The leftward shift in the fluctuation analyses suggests cooperativity postchannel clusters.

compared to *Slc26a5*$^{-/-}$ (fig. S4, A to C, blue) mice showed current with reduced magnitude (~1.7-fold; n = 7), 24-mV rightward shift in the half-activation voltage, and increased activation time constant (>10-fold). To attribute the observed I_{Kn} properties to a potential dependence of clustering on prestin expression, we compared the expression pattern of $K_v7.4$ in OHCs of *Slc26a5*$^{-/-}$ and their *Slc26a5*$^{+/+}$ littermates. $K_v7.4$ expression was scattered and supranuclear in *Slc26a5*$^{-/-}$ OHC membrane (fig. S4D), in contrast to the characteristic infranuclear consolidated expression in the *Slc26a5*$^{+/+}$ mice. Hence, $K_v7.4$ clustering and ultrafast electromechanical sensitivity appear to require prestin to develop, directly or indirectly.

Ultrafast electromechanical $K_v7.4$ gating in OHCs is predicted to markedly enhance the bandwidth, power efficiency, and tuning in the cochlea

We formulated a biophysically based model to examine potential consequences of ultrafast $K_v7.4$ mechanical gating on OHC electromotility and cochlear function. Details of the model are provided in

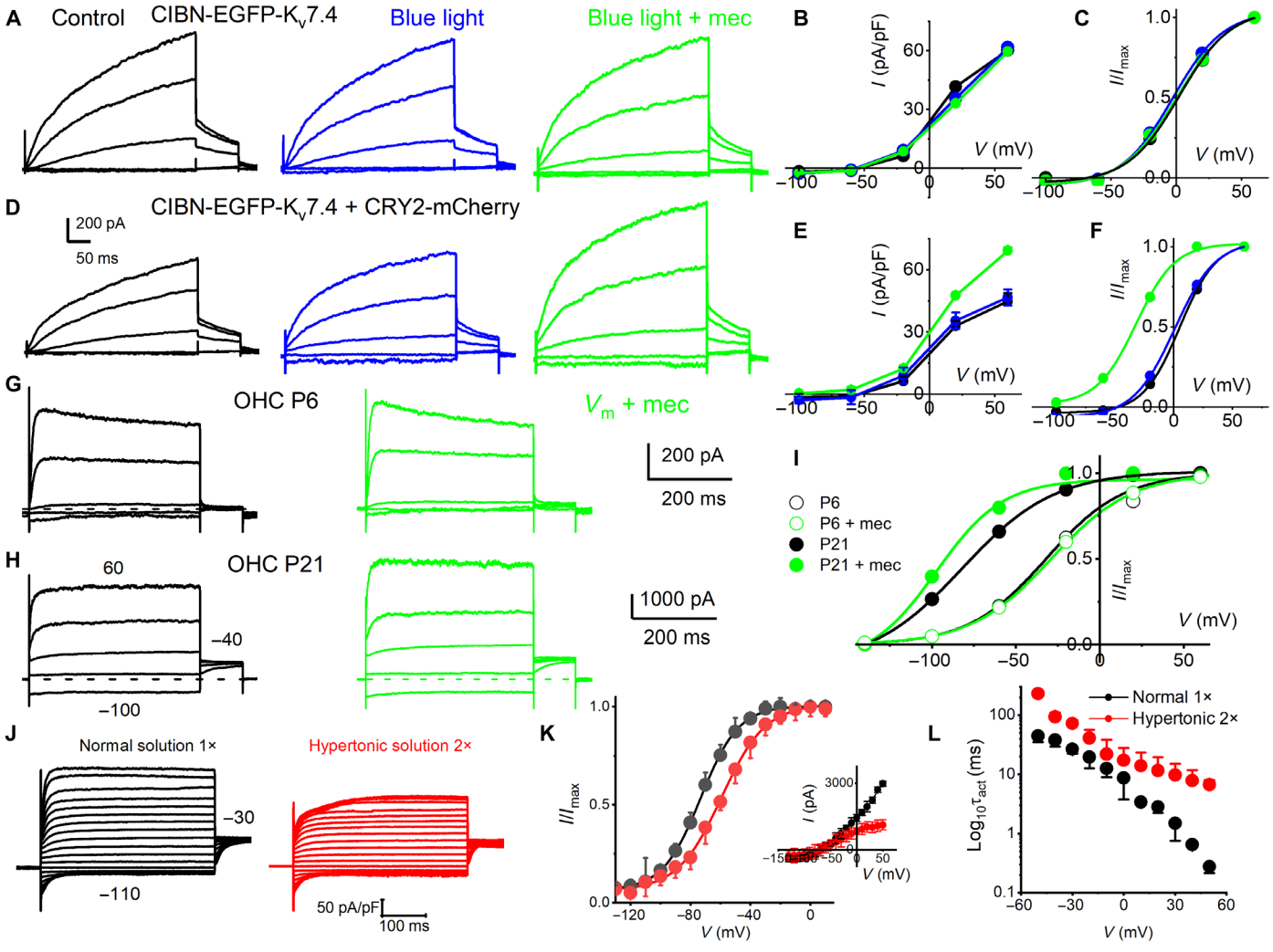

Fig. 5. CIBN-EGFP-K_v7.4 oligomerization and K_v7.4 consolidation in OHCs and mechanical sensitivity. (**A**) HEK 293 cells transfected with CIBN-EGFP-K_v7.4 for 48 hours. Outward CIBN-EGFP-K_v7.4 current traces (black) recorded from −60-mV holding potential, stepped from −100 to 50 mV, $\Delta V = 30$ mV. Current traces after exposure to blue light for ~5 min (blue traces) and blue light + mechanical (mec) (0.6 μm) cell-body displacement (green traces). (**B**) Current density (in pA/pF), voltage relations of summary data from seven cells, are shown. (**C**) The tail current at −40 mV and the $V_{1/2}$ (mV) and $1/k$ (V^{-1}) for activation curves: control, 0.6 ± 3.2 and 21.3 ± 3.5; after blue light, −2.6 ± 3.4 and 51.7 ± 6.1; and blue light + mec displacement, 5.5 ± 3.5 and 64.1 ± 4.4 ($n = 7$). Comparing $V_{1/2}$, there was significant difference at the $P < 0.05$ level for the population means $F(2,18) = 10$, $P = 0.001$. Post hoc comparisons test for control and blue light ($P = 0.2$). Blue light + mec displacement versus control means were significantly different ($P = 0.04$). Blue light + mec displacement versus blue-light means were significantly different ($P = 0.001$). Comparing $1/k$ at the $P < 0.05$ level for the population means $F(2,18) = 148$, $P = 0.0001$. Post hoc comparisons using the Tukey HSD test indicated that all three condition means were significantly different ($P = 0.0001$). (**D** to **F**) Results similar to that described in (A) to (C); HEK 293 cells were cotransfected with CIBN-EGFP-K_v7.4 and CRY2-mCherry. (D) τ_{act} abbreviated by ~2-fold after 5-min blue-light exposure (at 60 mV), and current density increased after 0.6-μm displacement (~1.3-fold). The tail current at −40 mV, and the $V_{1/2}$ (mV) and $1/k$ (V^{-1}) for activation curves were as follows: control, 0.6 ± 1.4 and 55.5 ± 10.8; after blue light, −4.5 ± 3.2 and 52.0 ± 9.7; and blue light + mec displacement, −32.6 ± 2.7 and 60.3 ± 8.1 ($n = 5$). Comparing $V_{1/2}$ at the $P < 0.05$ level for the population means $F(2,12) = 250$, $P = 0.0001$. Post hoc comparisons using the Tukey HSD for three conditions ($P = 0.2$). (**G**) Family of I_{Kn} traces (black) recorded from an OHC located at the 2-kHz frequency-place map of P6 mouse cochlea and after displacement of the basolateral cell wall by ~0.4 μm (green). Currents elicited from a holding voltage of −60 mV and the voltage steps from −130 to 50 mV, $\Delta V = 40$ mV. (**H**) Similar recording as in (G) from P21 OHC. A displacement of 0.4 μm sped up the τ_{act} [at a 60-mV step, τ_{act} (ms) was 7.6 ± 4.9 and 0.9 ± 0.5 ($n = 5$, $P < 0.05$)] before and after mec displacement, respectively. (**I**) At P21, mec displacement produced a leftward shift in the steady-state activation properties. The tail current at −40 mV and the $V_{1/2}$ (mV) and $1/k$ (V^{-1}) for activation curves were as follows: control, −81.8 ± 0.9 and 36.6 ± 7.7, and mec displacement, −97.3 ± 2.8 and 60.6 ± 12.4 ($n = 5$). Comparing $V_{1/2}$ ($P < 0.0001$) and $1/k$ ($P = 0.006$). Thus, 0.4-μm mec displacement produced a ~15 leftward shift in the voltage dependence and ~8-fold change in the τ_{act} in I_{Kn}. (**J**) I_{Kn} traces (black) from −60-mV holding voltage and voltage steps from −110 to 50 mV from P24 OHCs. In red traces are recordings from the same OHC ~5 min after bath perfusion of 630 mosmol (mannitol-based) solution. The current magnitude plummeted in five of seven OHCs. For the remaining two OHCs, the current magnitude was unchanged after hypertonic solution. (**K**) The summary data from five OHCs are shown as inset in the current-voltage relationship. $V_{1/2}$ for I_{Kn} in P24 OHC was −73.2 ± 3.3 mV; the voltage sensitivity at half-activation, $1/k$, was 79.4 ± 9.3 V^{-1} ($n = 5$); posthypertonic solution (2×) was −59.3 ± 3.7 mV and $1/k$ was 68.5 ± 8.8 V^{-1} ($n = 5$). Comparing $V_{1/2}$ ($P = 0.0002$) and $1/k$ ($P = 0.09$). (**L**) Changes in the τ_{act} relative to step voltages for I_{Kn} in normal and hypertonic solution ($n = 5$ OHCs).

the Supplementary Materials. We found a simple transition-state model (*24*) consisting of three closed states, and one open state (Fig. 6A) was sufficient to reproduce the significant effects of clustering, voltage, and mechanical stress on whole-cell currents both in HEK 293 cells (fig. S5) and in OHCs (Fig. 6). The cell membrane was modeled using the standard approach with variable ionic conductances as well as linear and nonlinear (piezoelectric) capacitance (Fig. 6B). After confirming the accuracy of the model to predict electromechanical gating and currents measured in adult OHCs (Fig. 6, C to E), we inserted the $K_v7.4$ channel model into a piezoelectric model of an OHC based on (*25*). The OHC was also coupled to a simplified spring-mass-damper model of the local cochlear load, simulating the OHC location between Deiters' cell at the base and the tectorial membrane at the apex (Fig. 6F) (*5*, *26*). The coupled model was used to predict the frequency response and power efficiency of an OHC from the 3-kHz region of the cochlea [based on the first harmonic extracted from nonlinear time-domain simulations (Fig. 6, G and H)]. Ultrafast electromechanical gating of $K_v7.4$ arising from the cooperativity of channels is predicted by the simulations to endow OHCs with the ability to sense and react to the cochlear load on a cycle-by-cycle basis. The ability to sense the mechanical load adds to the emergent tuning of the cochlea (Fig. 6G, red) and improves the electrical-to-mechanical power conversion of OHCs by a form of dynamic impedance matching (Fig. 6H, red). Although the OHC electromotility gain is sensitive to specific model parameters (table S1), the prediction that $K_v7.4$ mechanosensitivity tunes OHC electromechanics to match the cochlear load is robust. Thus, the electromechanical properties of $K_v7.4$ channels are likely essential to OHC function and tuned cochlear amplification.

DISCUSSION

Results demonstrate that $K_v7.4$ channels acquire ultrafast electromechanical gating in mature OHCs through intrachannel cooperativity. Ultrafast kinetics develop in OHCs during maturation of hearing as $K_v7.4$ channels consolidate in high-density clusters at the basal pole. Intrachannel cooperativity leading to enhanced electromechanical sensitivity is a property of $K_v7.4$ channels and could also be induced, in vitro, in HEK 293 cells using an optogenetic approach to coalesce channels into clusters. In mature OHCs, the magnitude and kinetics of I_{Kn} both increase with CF location from apex to base, demonstrating that $K_v7.4$ function is titrated in OHCs to match the local tonotopic requirements of the cochlea through both expression (setting I_{Kn} magnitude) and cooperativity (setting I_{Kn} kinetics). This tonotopic distribution augments previously established distributions in MET currents, prestin expression, cell electromechanics, and morphology reported previously (*27*), clearly confirming the fact that individual OHCs are specialized to match the requirements at their specific location in the cochlea.

Our findings of $K_v7.4$ cooperativity are in conceptual agreement with recent reports demonstrating voltage-gated K^+ and Ca^{2+} channel mutations resulting in properties inconsistent with the expectations of individual channels with distinct autonomous voltage-dependent gating (*28*, *29*). Similar accounts were described for the hyperpolarization-activated cyclic nucleotide-gated channels, where the elementary properties of single-channel events were compared to membrane patches containing multiple channels (*30*). Intrachannel cooperativity does not operate alone in OHCs but appears to combine with other factors to set the kinetics and highly hyperpolarized half-activation voltage of I_{Kn} (*31*). $K_v7.4$ accessory subunits regulate the voltage-dependent activation, which would be absent in the cell line and may explain why chemically induced $K_v7.4$ aggregation does not shift the half-activation as much as development in OHCs (Figs. 2C and 4D).

Mechanosensitivity of $K_v7.4$ revealed here emerges with cooperativity, provides OHCs with the ability to sense the external load acting on the cell, and is likely to be extremely important to OHC function in the cochlea. The reason mechanosensitivity is so essential is most clearly illustrated in Fig. 6, where the displacement of an OHC from the 3-kHz location is shown as a function of frequency in Fig. 6G under three conditions: $K_v7.4$ null (black), $K_v7.4$ tonic DC conductance only (blue, dashed), and $K_v7.4$ full electromechanical function (red). All three curves are subject to the same overdamped cochlear load and plotted relative to the magnitude of a sinusoidal MET current input. As expected, adding a tonic DC conductance of $K_v7.4$ at rest shifts the OHC corner frequency up (*13*), but this comes at the expense of sensitivity (gain, Fig. 6G, blue dashed line), making it unclear what advantage a leaky DC conductance would provide for hearing other than the partial flattening of the OHC gain. In sharp contrast, ultrafast cycle-by-cycle mechanosensitivity introduced a marked shift in the corner frequency and increased the gain at CF (Fig. 6G, asterisk). The tuning of the OHC emerged when operating in the context of the cochlear load. The tuning arises because the stress acting on $K_v7.4$ is dominated by the elastic load at low frequencies (below CF), but dominated by the mass load at high frequencies (above CF). This causes a sign reversal of the stress relative to the cell displacement, and hence, the electrical contribution of $K_v7.4$ reverses from a leak conductance at low frequencies to a counterbalancing current at high frequencies (Fig. 6I). Thus, the best frequency lies between these two extremes: the optimal state of the electromechanical force (Fig. 6G, asterisk). The net effect is that OHCs react to the cochlear load and automatically adjust their response to deliver the highest magnitude displacement at the CF frequency. Hence, the mechanosensitivity of cooperative $K_v7.4$ channels is predicted to markedly attenuate the low-frequency response while amplifying the response at CF. This effect requires the OHC to work in the context of the cochlear load and would not be seen in isolated cells without introducing the appropriate load. The cochlear load was overdamped in the simulations, but the mechanical response looks underdamped. Conversion to an underdamped system by mechanosensitivity of $K_v7.4$ is likely the elusive mechanism used by OHCs to cancel viscous losses, long thought to occur in the active cochlea, but with unclear origins (*32*–*34*).

Mechanosensitivity is also predicted to optimize the efficiency of OHCs. The endolymphatic potential is the battery that drives MET currents and provides the electrical power input to OHCs. This electrical power is converted to mechanical power by the piezoelectric-like motor of the lateral wall (fig. S5), and the ratio of the two provides the power efficiency. Like skeletal muscle cells, the power efficiency in OHCs is optimized at a specific velocity and force that match the impedance of the load to the resistance of the cell (*25*). One might surmise that the tonic leak conductance introduced by $K_v7.4$ would shunt input power and reduce efficiency. This is precisely the expected occurrence at low frequencies when I_{Kn} serves as the leak current (Fig. 6H). However, as the stress acting on the channel begins to shift, the mechanosensitive current causes the efficiency to reach nearly 80% (Fig. 6, G and H, ω_d), a value perhaps higher than any known biological motor and predicted to be more than double the efficiency of an OHC lacking $K_v7.4$ mechanosensitivity.

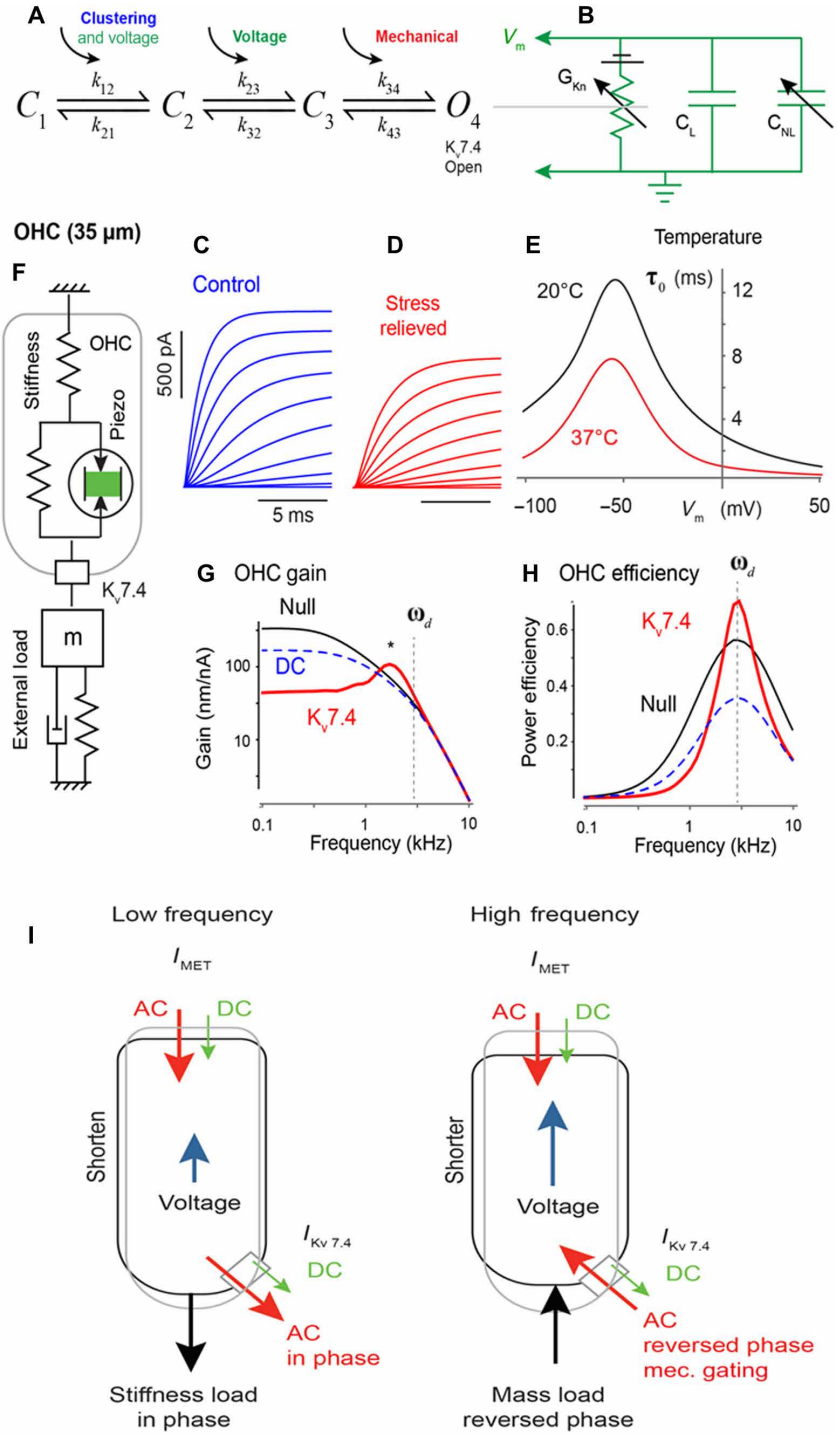

Fig. 6. Biophysical model and potential contributions of K_v7.4 to OHC function. (**A**) Four-state chemical kinetic model of K_v7.4 gating of conductance based on Eyring's transition state theory (see the Supplementary Materials). The model accounts for clustering through entropy of the first transition, voltage gating through two transitions, and mechanical gating through enthalpy of the final transition. (**B**) The K_v7.4 conductance is inserted into a passive HEK model or an active piezoelectric model of the OHC (F). (**C** and **D**) Simulated voltage-clamp currents in K_v7.4-transfected HEK cells under control, oligomerized, and stress-relieved conditions. (**E**) Simulated voltage-clamp currents and activation kinetics based on OHC parameters (table S1). Effects of temperatures 20°C (black) and 37°C (red) on time constant of channel openings (τ_o). (**F**) The mechanical portion of the OHC model with an external load matched to the cell. (**G**) OHC tuning curves for a model cell from the 3-kHz region of the cochlea in the control condition (Null), after adding a DC K_v7.4 conductance (blue dashed line), and after adding mechanovoltage-sensitive K_v7.4 conductance (red solid line). (**H**) The power efficiency of the OHC is predicted to be increased by mechanovoltage-sensitive K_v7.4 (red solid line) while reduced by a passive DC conductance. (**I**) Schematic diagram showing conditions of an OHC at low (left) and high (right) frequency. At high frequency, viscous mass predominates, and there is a 180° phase switch resulting mainly from the mechanical gating of the K_v7.4 channel. I_{MET}, mechanoelectrical transducer current. $I_{Kv7.4}$, K_v7.4 current.

MATERIALS AND METHODS

The Animal Care and Ethical Committee of the University of Nevada, Reno approved the use of animals in this study. OHCs from equal numbers of male and female C57BL/6 J mice (ages P4 to P48; the Jackson Laboratory) were used in an acutely dissected organ of Corti. The tissue was mounted under an insect pin glued to a coverslip for electrophysiological recordings.

Dissection of the organ of Corti

The organ of Corti was dissected from equal numbers of male and female postnatal (P4 to P48) C57BL/6 J mice cochlea. Mice were euthanized, and the temporal bones were removed for further dissection in standard extracellular solution, which contained 144 mM NaCl, 0.7 mM $NaHPO_4$, 5.8 mM KCl, 0.9 mM $MgCl_2$, 10 mM Hepes, 1.3 mM $CaCl_2$, and 5.6 mM glucose (pH was adjusted to 7.4). Amino acids and vitamins for Eagle's minimal essential medium were added from concentrates (Invitrogen). The bone surrounding the cochlea was dissected away; the stria vascularis, lateral cochlear wall, and tectorial membrane were removed. The cochlear explant was transferred to a chamber on an upright microscope (Olympus BX50WI, 60× WI objective) for electrophysiological experiments.

Immunofluorescence confocal microscopy of OHCs

Cochlear epithelia were fixed by 4% paraformaldehyde in phosphate-buffered saline (PBS) for ~30 min at 4°C and then washed three times with PBS for 5 min. After being treated with 0.4% Triton X-100 in PBS for 15 min, the tissues were washed and treated with −20°C methanol for 10 min and then washed and treated with antibody [1:100 dilution for anti-K_v7.4 (Sigma-Aldrich) and 1:100 for anti-myosin 7A (Sigma-Aldrich) antibodies]. Immunofluorescence-labeled samples were examined by using Zeiss LSM 510 confocal laser scanning microscopy. To ascertain, in double or triple staining, that there was no overlap between the detection of the fluorochromes, singly labeled OHCs were imaged under identical conditions to those used for dual/triple-labeled probes to confirm proper signal isolation of each channel. Control experiments performed by preincubation of the primary antibody with the respective antigenic peptide (1:1) did not show positive staining under the same experimental conditions used. Identical settings were used for all specimens. Z-stack sections were collected, and 2/3/4-D static and motion images were reconstructed offline using image visualization and analysis software (Imaris, Bitplane, Oxford Instruments).

Whole-cell voltage-clamp recordings

Patch-clamp experiments were performed in standard whole-cell configurations using an Axopatch 200B amplifier (Axon Instruments). Patch pipettes had a resistance of 1 to 2 megohms when filled with an internal solution consisting of 142 mM KCl, 5 mM Hepes, 1 mM EGTA, 0.1 mM $CaCl_2$, 3.5 mM $MgCl_2$, and 2.5 mM MgATP (pH adjusted to 7.3 with KOH). The extracellular solution consisted of 144 mM NaCl, 0.7 mM $NaHPO_4$, 5.8 mM KCl, 0.9 mM $MgCl_2$, 10 mM Hepes, 1.3 mM $CaCl_2$, and 5.6 mM glucose (pH was adjusted to 7.4 with NaOH). Amino acids and vitamins for Eagle's minimal essential medium were added from concentrates (Invitrogen). Experiments were performed at temperatures ranging from room temperature to 20° to 37°C using a bipolar temperature controller (Warner Instruments). Currents were sampled at 50 or 20 kHz and filtered at 5 or 2 kHz with a 16-bit A/D converter (Digidata 1322A, Axon Instruments). Liquid junction potentials were measured (2.1 ± 0.7 mV, $n = 89$) and corrected online. Access resistance in series with the recording electrode was measured and compensated >90%, and recording from OHCs with voltage errors greater than 2 mV were discarded from analyses. The stock solutions of lino (Sigma-Aldrich) were made in dimethyl sulfoxide (DMSO) and stored at −20°C. The final concentration of DMSO in the recording bath solution was 0.0001%. This concentration of DMSO had no effects on outward currents.

For whole-cell voltage-clamp recordings made in transfected HEK 293 cells, the bath solution contained the following: 145 mM NaCl, 4 mM KCl, 0.5 mM $MgCl_2$, 1.8 mM $CaCl_2$, 10 mM Hepes, and 10 mM glucose (pH 7.4 with NaOH). The pipettes were filled with a solution consisting of 112 mM KCl, 2 mM $MgCl_2$, 0.1 mM $CaCl_2$, 1 mM EGTA, 10 mM Hepes, 5 mM K_2ATP, and 0.5 mM Na_2GTP (pH 7.35 with KOH).

Gating current recordings

Gating currents were recorded from HEK 293 cells transfected with EGFP, CRY2-mCherry, CIBN-EGFP-K_v7.4, and CRY2-mCherry, using pipette solution containing 145 mM TEAOH, 0.5 mM $MgCl_2$, 0.1 mM $CaCl_2$, 1 mM EGTA, 7 mM TEACl, and 10 mM Hepes (pH 7.25 with glutamic acid). The external solution consisted of 145 mM TEAOH, 3 mM $BaCl_2$, 0.5 mM $MgCl_2$, 0.5 mM $CaCl_2$, 10 mM Hepes, and 5 mM glucose (pH 7.4 with glutamic acid). Experiments were performed under pre– and post–blue-light illumination (see below). Gating currents were elicited using ~5-ms voltage steps from −100 to 60 mV in 10-mV increments. Current outputs were low-pass–filtered at 1 kHz and acquired at 20 kHz. Experiments were performed using Clampex 8 (Axon Instruments) acquisition software. Leak subtraction was performed based on a P/7 protocol.

Cryptochrome-mediated K_v7.4 clusters and immunofluorescence in HEK 293 cells

pCIBN-pmGFP (#26867) and CRY2olig-mCherry (#60032) plasmids were purchased from Addgene. To generate pCIBN-EGFP–(flexible linker)–K_v7.4 clone, pCIBN-pmGFP was linearized by Age I and Eco RI restriction enzymes, and the pmGFP segment was removed. Polymerase chain reaction–generated EGFP and K_v7.4 fragments overlapping homologous sequences at the ends were assembled to the vector by using the Choo-Choo cloning system (MCLAB, CA), under the manufacturer's instructions. Primer sequences to generate the fragments are listed below. EGFP with a flexible linker (SRGGSGGSGGSGGSGGRS): 5-EGFP-**GGA TTA TAT TCA TGT ACC GGT** CGC CAC CAT GGT GAG CAA and 3-EGFP-***GCT GCG GCC GCC GCT*** **GCC GCC GCT GCC GCC GCT GCC GCC GCT GCC GCC GCG GCT** ACC CTT ATA CAG CTC GTC were used. For K_v7.4 fragment: 5-Q4 AGC GGC GGC CGC AGC ATG GCC GAG GCC CCT CCC and 3-Q4 **G TCG ACT GCA GAA TTC** TCA GTC CAT GTT GGT GGA CAC. The clone was verified by sequencing.

HEK 293 cells were obtained from the American Type Culture Collection. The cells were maintained in Dulbecco's modified Eagle's medium containing 10% fetal bovine serum (Invitrogen) at 37°C in a CO_2 incubator. Transfections were performed using Lipofectamine 2000 following the protocol of the manufacturer, and 1 μg of total DNA per 35-mm dish was used.

We used an optogenetic light-induced protein cluster system based on CRY2 and CIB1 proteins of *Arabidopsis thaliana* (*17*) to mediate K_v7.4 clusters. Cells were cotransfected with the N-terminal region of CIB1 (EGFP-CIBN) and mCherry-CRY2 at a 1:1 molar ratio.

Thirty-six to 48 hours after transfection, cells were illuminated with blue light, which promotes binding of CRY2 to the CIBN to mediate $K_v7.4$ clusters. Control experiments were conducted to determine whether the fusion channel protein, EGFP-CIBN-$K_v7.4$, has functional properties similar to those of $K_v7.4$ channel alone (fig. S2).

Confocal microscopy and FRAP

HEK 293 cells were transfected with CRY2olig-mCherry and CIBN-$K_v7.4$-EGFP using Lipofectamine 2000 (Life Technologies, Carlsbad, CA). Live cells were imaged using a 63× oil objective on a Zeiss LSM 700 confocal laser scanning microscope. All cells were selected without exposure to blue light. Baseline images were taken with rapid exposure times (less than 4 s per frame) to measure baseline intensity and limit excitation before the experiment. For FRAP experiments, cells were excited with blue light; mCherry and EGFP emissions were collected over time. Imaging and analyses were performed using Zen 2009, ImageJ, and Imaris software. All analyses were performed in a blinded fashion.

FRAP experiments were performed at room temperature (~21°C) with a Zeiss LSM 510 META confocal microscope and MultiTime software. Regions of interest (ROIs) were randomly selected from the cell membrane. The time course of colocalization of EGFP and mCherry, as a correlate for channel clusters, was determined by comparing data from before and after blue-light illumination. Pre- and postbleach images were acquired using laser beam scanning once every 10 s with the 568-nm excitation wavelength. For photobleaching, the laser was set to 100% transmission. The fluorescence intensity was measured in the bleached area as a function of time (t), and mean background values were determined outside the ROI and subtracted from all intensity data points before further analysis to correct overall photobleaching. The average fluorescence intensity within bleached ROIs was normalized to prebleach intensity for each time point. Experiments were performed on a Zeiss microscope swept field confocal system equipped with a 488-nm laser line and a Plan Apo 63× 1.45 numerical aperture oil immersion objective.

Forty-eight hours after transfection, K^+ currents were recorded in voltage-clamp mode. Two to 3 min after initiating electrical access to transfected HEK 293 cells, cells were exposed to a blue-light pulse at different exposure times to induce $K_v7.4$ clusters. In HEK 293 cells, K^+ currents were recorded before and after blue-light illumination in response to 2-s depolarizing pulse from a holding voltage of −70 mV to voltages ranging from −120 to 60 mV, using 10-mV increments.

Antibodies

The following primary antibodies were used: (i) anti-$K_v7.4$ antibody (Alomone, APC-164), a polyclonal antibody raised in rabbits against a purified peptide corresponding to amino acid residues 594 to 607 of mouse $K_v7.4$ located at the C terminus, and (ii) anti-myosin 7A antibody (Proteus BioSciences, 25-6790). Secondary antibodies used were as follows: anti-mouse peroxidase-conjugated secondary antibody (Amersham), anti-rabbit peroxidase-conjugated secondary antibodies (Abcam), goat anti-rabbit immunoglobulin G (IgG)–Cy3 conjugate (Jackson ImmunoResearch, 111-095-045), goat polyclonal antibodies to mouse IgG-Cy3 conjugate (Jackson ImmunoResearch, 111-165-003), donkey anti-goat IgG–fluorescein isothiocyanate (FITC) conjugate (Jackson ImmunoResearch, 705-095-147), and goat anti-rabbit IgG-Cy3 conjugate (Jackson ImmunoResearch, 11-165-045).

Data analysis

All data analyses were performed offline with Clampfit 8 (Axon Instruments) and Microcal Origin (OriginLab, version 8). The number of animals and cells used are indicated in the figure legends. Current magnitudes were measured using averages of the steady-state, tail (deactivation), and peak level detection routine in the pClamp software. Whole-cell K^+ currents were normalized and plotted against the step potential. Continuous curves were generated from the Boltzmann function $I/I_{max} = (1 + (\exp(V_{1/2} - V)/k_m))$, where $V_{1/2}$ is the half-activation voltage, $k_m = RT/zF$ is the slope factor, $1/k_m$ is the voltage sensitivity at half-activation, I is the magnitude of the current, and I_{max} denotes the maximum current size. Gating currents were derived from the integral between 0 and 600 μs after the test voltage (V) to determine the net charge (Q) movement. Q-V relationships were fit with a Boltzmann function: $Q = Q_{max}/(1 - \exp.(-zF(V - V_{1/2})/RT))$, where Q_{max} is the maximum charge, z is the voltage dependence of activation, $V_{1/2}$ is the half-activation voltage, T is the absolute room temperature (294 K), F is Faraday's constant, and R is the universal gas constant. Q_{max}, $V_{1/2}$, and z were determined by using the iterative process in Origin software. The lateral surface area of OHCs was calculated as described previously (*35*). We assumed OHC cell shape as a cylinder with length l and a hemisphere of diameter d. The estimated lateral surface area (S) was computed as $S = \pi d(l - d/2)$. Statistical analysis was performed using a paired or unpaired t test and analysis of variance (ANOVA) with significance taken as $P < 0.05$.

SUPPLEMENTARY MATERIALS

Supplementary material for this article is available at http://advances.sciencemag.org/cgi/content/full/6/15/eaba1104/DC1

View/request a protocol for this paper from *Bio-protocol*.

REFERENCES AND NOTES

1. C. E. Carr, C. Köppl, Coding interaural time differences at low best frequencies in the barn owl. *J. Physiol. Paris* **98**, 99–112 (2004).
2. W. E. Brownell, C. R. Bader, D. Bertrand, Y. de Ribaupierre, Evoked mechanical responses of isolated cochlear outer hair cells. *Science* **227**, 194–196 (1985).
3. G. Frank, W. Hemmert, A. W. Gummer, Limiting dynamics of high-frequency electromechanical transduction of outer hair cells. *Proc. Natl. Acad. Sci. U.S.A.* **96**, 4420–4425 (1999).
4. N. P. Cooper, A. Vavakou, M. van der Heijden, Vibration hotspots reveal longitudinal funneling of sound-evoked motion in the mammalian cochlea. *Nat. Commun.* **9**, 3054 (2018).
5. J. Santos-Sacchi, K. H. Iwasa, W. Tan, Outer hair cell electromotility is low-pass filtered relative to the molecular conformational changes that produce nonlinear capacitance. *J. Gen. Physiol.* **151**, 1369–1385 (2019).
6. J. Santos-Sacchi, W. Tan, The frequency response of outer hair cell voltage-dependent motility is limited by kinetics of prestin. *J. Neurosci.* **38**, 5495–5506 (2018).
7. J. Zheng, W. Shen, D. Z. Z. He, K. B. Long, L. D. Madison, P. Dallos, Prestin is the motor protein of cochlear outer hair cells. *Nature* **405**, 149–155 (2000).
8. A. J. Hudspeth, The cellular basis of hearing: The biophysics of hair cells. *Science* **230**, 745–752 (1985).
9. A. J. Ricci, H. J. Kennedy, A. C. Crawford, R. Fettiplace, The transduction channel filter in auditory hair cells. *J. Neurosci.* **25**, 7831–7839 (2005).
10. D. C. Mountain, A. E. Hubbard, A piezoelectric model of outer hair cell function. *J. Acoust. Soc. Am.* **95**, 350–354 (1994).
11. H. Davis, An active process in cochlear mechanics. *Hear. Res.* **9**, 79–90 (1983).
12. D. T. Kemp, Stimulated acoustic emissions from within the human auditory system. *J. Acoust. Soc. Am.* **64**, 1386–1391 (1978).
13. S. L. Johnson, M. Beurg, W. Marcotti, R. Fettiplace, Prestin-driven cochlear amplification is not limited by the outer hair cell membrane time constant. *Neuron* **70**, 1143–1154 (2011).
14. W. Marcotti, C. J. Kros, Developmental expression of the potassium current IK,n contributes to maturation of mouse outer hair cells. *J. Physiol.* **520**, 653–660 (1999).

15. T. Kharkovets, K. Dedek, H. Maier, M. Schweizer, D. Khimich, R. Nouvian, V. Vardanyan, R. Leuwer, T. Moser, T. J. Jentsch, Mice with altered KCNQ4 K^+ channels implicate sensory outer hair cells in human progressive deafness. *EMBO J.* **25**, 642–652 (2006).
16. A. Taslimi, J. D. Vrana, D. Chen, S. Borinskaya, B. J. Mayer, M. J. Kennedy, C. L. Tucker, An optimized optogenetic clustering tool for probing protein interaction and function. *Nat. Commun.* **5**, 4925 (2014).
17. M. J. Kennedy, R. M. Hughes, L. A. Peteya, J. W. Schwartz, M. D. Ehlers, C. L. Tucker, Rapid blue-light–mediated induction of protein interactions in living cells. *Nat. Methods* **7**, 973–975 (2010).
18. R. E. Dixon, C. Yuan, E. P. Cheng, M. F. Navedo, L. F. Santana, Ca^{2+} signaling amplification by oligomerization of L-type $Ca_v1.2$ channels. *Proc. Natl. Acad. Sci. U.S.A.* **109**, 1749–1754 (2012).
19. M. E. Gomez-Casati, E. Katz, E. Glowatzki, M. I. Lioudyno, P. Fuchs, A. B. Elgoyhen, Linopirdine blocks $\alpha9\alpha10$-containing nicotinic cholinergic receptors of cochlear hair cells. *J. Assoc. Res. Otolaryngol.* **5**, 261–269 (2004).
20. M. G. Leitner, A. Feuer, O. Ebers, D. N. Schreiber, C. R. Halaszovich, D. Oliver, Restoration of ion channel function in deafness-causing KCNQ4 mutants by synthetic channel openers. *Br. J. Pharmacol.* **165**, 2244–2259 (2012).
21. H. J. Kim, P. Lv, C.-R. Sihn, E. N. Yamoah, Cellular and molecular mechanisms of autosomal dominant form of progressive hearing loss, DFNA2. *J. Biol. Chem.* **286**, 1517–1527 (2011).
22. O. Yifrach, R. MacKinnon, Energetics of pore opening in a voltage-gated K^+ channel. *Cell* **111**, 231–239 (2002).
23. J.-M. Chambard, J. F. Ashmore, Regulation of the voltage-gated potassium channel KCNQ4 in the auditory pathway. *Pflügers Arch.* **450**, 34–44 (2005).
24. H. Eyring, The activated complex in chemical reactions. *J. Chem. Phys.* **3**, 107–115 (1935).
25. R. D. Rabbitt, S. Clifford, K. D. Breneman, B. Farrell, W. E. Brownell, Power efficiency of outer hair cell somatic electromotility. *PLOS Comput. Biol.* **5**, e1000444 (2009).
26. D. Ó Maoiléidigh, A. J. Hudspeth, Effects of cochlear loading on the motility of active outer hair cells. *Proc. Natl. Acad. Sci. U.S.A.* **110**, 5474–5479 (2013).
27. S. S. Gao, R. Wang, P. D. Raphael, Y. Moayedi, A. K. Groves, J. Zuo, B. E. Applegate, J. S. Oghalai, Vibration of the organ of Corti within the cochlear apex in mice. *J. Neurophysiol.* **112**, 1192–1204 (2014).
28. G. E. Kim, L. K. Kaczmarek, Emerging role of the KCNT1 Slack channel in intellectual disability. *Front. Cell. Neurosci.* **8**, 209 (2014).
29. C. M. Moreno, R. E. Dixon, S. Tajada, C. Yuan, X. Opitz-Araya, M. D. Binder, L. F. Santana, Ca^{2+} entry into neurons is facilitated by cooperative gating of clustered $Ca_v1.3$ channels. *eLife* **5**, e15744 (2016).
30. J. P. Dekker, G. Yellen, Cooperative gating between single HCN pacemaker channels. *J. Gen. Physiol.* **128**, 561–567 (2006).
31. D. J. Jagger, J. F. Ashmore, Regulation of ionic currents by protein kinase A and intracellular calcium in outer hair cells isolated from the guinea-pig cochlea. *Pflügers Arch.* **437**, 409–416 (1999).
32. T. Gold, Hearing. II. The physical basis of the action of the cochlea. *Proc. R. Soc. Lond. B Biol. Sci.* **135**, 492–498 (1997).
33. J. Ashmore, Biophysics of the cochlea—Biomechanics and ion channelopathies. *Br. Med. Bull.* **63**, 59–72 (2002).
34. S. T. Neely, D. O. Kim, A model for active elements in cochlear biomechanics. *J. Acoust. Soc. Am.* **79**, 1472–1480 (1986).
35. I. A. Belyantseva, G. I. Frolenkov, J. B. Wade, F. Mammano, B. Kachar, Water permeability of cochlear outer hair cells: Characterization and relationship to electromotility. *J. Neurosci.* **20**, 8996–9003 (2000).
36. J. Santos-Sacchi, Reversible inhibition of voltage-dependent outer hair cell motility and capacitance. *J. Neurosci.* **11**, 3096–3110 (1991).
37. R. Latorre, G. Vargas, G. Orta, S. Brauchi, Voltage and temperature gating of thermoTRP channels, in *TRP Ion Channel Function in Sensory Transduction and Cellular Signaling Cascades*, W. Liedtke, S. Heller, Eds. (CRC Press/Taylor & Francis, 2007), chap. 21.
38. F. Yang, J. Zheng, High temperature sensitivity is intrinsic to voltage-gated potassium channels. *eLife* **3**, e03255 (2014).
39. W. Y. Yang, M. Gruebele, Folding at the speed limit. *Nature* **423**, 193–197 (2003).
40. R. D. Rabbitt, A. M. Brichta, H. Tabatabaee, P. J. Boutros, J. Ahn, C. C. Della Santina, L. A. Poppi, R. Lim, Heat pulse excitability of vestibular hair cells and afferent neurons. *J. Neurophysiol.* **116**, 825–843 (2016).

Acknowledgments: We thank members of our laboratory, J. Hudspeth, J. Santos-Sacchi, W. Brownell, M. Sanguinetti, J. Holt, H. von Gersdoff, L. Trussell, and I. Russell for constructive and supportive comments on this manuscript. **Funding:** This work was supported by grants from the NIH, including NIH R01 DC016099, NIH R01 DC015135, NIH R01 DC015252, NIH P01 AG051443, and NIH R01 AG060504 to E.N.Y.; NIH R01 DC006685 to R.D.R.; NIH R01 HL085727, NIH R01 HL085844, NIH R01 HL137228, and VA Merit Review Grants I01 BX000576 and I01 CX001490 to N.C.; and NIH R56 HL138392 to X.-D.Z. H.A.L. was supported by Predoctoral Fellowship from NIH/NHLBI Institutional Training Grant in Basic and Translational Cardiovascular Science NIH T32 HL086350 and NIH F31 HL136120 Predoctoral Awards. **Author contributions:** E.N.Y., R.D.R., N.C., and H.J.K. designed the research; M.C.P.-F., J.H.L., S.P., X.-D.Z., W.W., C.-R.S., H.A.L., V.Y.-Y., N.C., R.D.R., H.J.K., and E.N.Y. performed experiments, analyzed data, and wrote the manuscript; and M.C.P.-F., J.H.L., S.P., X.-D.Z., W.W., C.-R.S., V.T., H.J.K., V.Y.-Y., N.C., R.D.R., and E.N.Y. performed quantitative analyses of the project. In addition, R.D.R. wrote the code for the simulation. All authors read and approved the final manuscript. **Competing interests:** The authors declare that they have no competing interests. **Data and materials availability:** All data needed to evaluate the conclusions in the paper are present in the paper and/or the Supplementary Materials. Additional data related to this paper may be requested from the authors.

Submitted 5 November 2019
Accepted 14 January 2020
Published 8 April 2020
10.1126/sciadv.aba1104

Citation: M. C. Perez-Flores, J. H. Lee, S. Park, X.-D. Zhang, C.-R. Sihn, H. A. Ledford, W. Wang, H. J. Kim, V. Timofeyev, V. Yarov-Yarovoy, N. Chiamvimonvat, R. D. Rabbitt, E. N. Yamoah, Cooperativity of $K_v7.4$ channels confers ultrafast electromechanical sensitivity and emergent properties in cochlear outer hair cells. *Sci. Adv.* **6**, eaba1104 (2020).